



Highly specific characterization and discrimination of monosodium urate crystals in gouty arthritis based on aggregation-induced emission luminogens

Wenjuan Wang¹ · Guiquan Zhang^{2,3} · Ziyi Chen¹ · Hanlin Xu¹ · Bohan Zhang⁵ · Rong Hu^{2,3,4} · Anjun Qin^{2,3} · Yinghui Hua¹

Received: 28 April 2023 / Accepted: 19 June 2023 / Published online: 13 October 2023

© Zhejiang University Press 2023

Abstract

Existing technologies used to detect monosodium urate (MSU) crystals for gout diagnosis are not ideal due to their low sensitivity and complexity of operation. The purpose of this study was to explore whether aggregation-induced emission luminogens (AIEgens) can be used for highly specific imaging of MSU crystals to assist in the diagnosis of gout. First, we developed a series of luminogens (i.e., tetraphenyl ethylene (TPE)-NH₂, TPE-2NH₂, TPE-4NH₂, TPE-COOH, TPE-2COOH, TPE-4COOH, and TPE-Ketoalkyne), each of which was then evenly mixed with MSU crystals. Next, optimal fluorescence imaging of each of the luminogens was characterized by a confocal laser scanning microscope (CLSM). This approach was used for imaging standard samples of MSU, hydroxyapatite (HAP) crystals, and mixed samples with 1:1 mass ratio of MSU/HAP. We also imaged samples from mouse models of acute gouty arthritis, HAP deposition disease, and comorbidities of interest. Subsequently, CLSM imaging results were compared with those of compensated polarized light microscopy, and we assessed the biosafety of TPE-Ketoalkyne in the RAW264.7 cell line. Finally, CLSM time series and three-dimensional imaging were performed on MSU crystal samples from human gouty synovial fluid and tophi. As a promising candidate for MSU crystal labeling, TPE-Ketoalkyne was found to detect MSU crystals accurately and rapidly in standard samples, animal samples, and human samples, and could precisely distinguish gout from HAP deposition disease. This work demonstrates that TPE-Ketoalkyne is suitable for highly specific and timely imaging of MSU crystals in gouty arthritis and may facilitate future research on MSU crystal-related diseases.

Wenjuan Wang, Guiquan Zhang, and Ziyi Chen contributed equally to this work.

✉ Rong Hu
hurong@usc.edu.cn

✉ Anjun Qin
msqinaj@scut.edu.cn

✉ Yinghui Hua
hua_cosm@aliyun.com

¹ Department of Sports Medicine, Huashan Hospital, Fudan University, Shanghai 200040, China

² State Key Laboratory of Luminescent Materials and Devices, Guangdong Provincial Key Laboratory of Luminescence

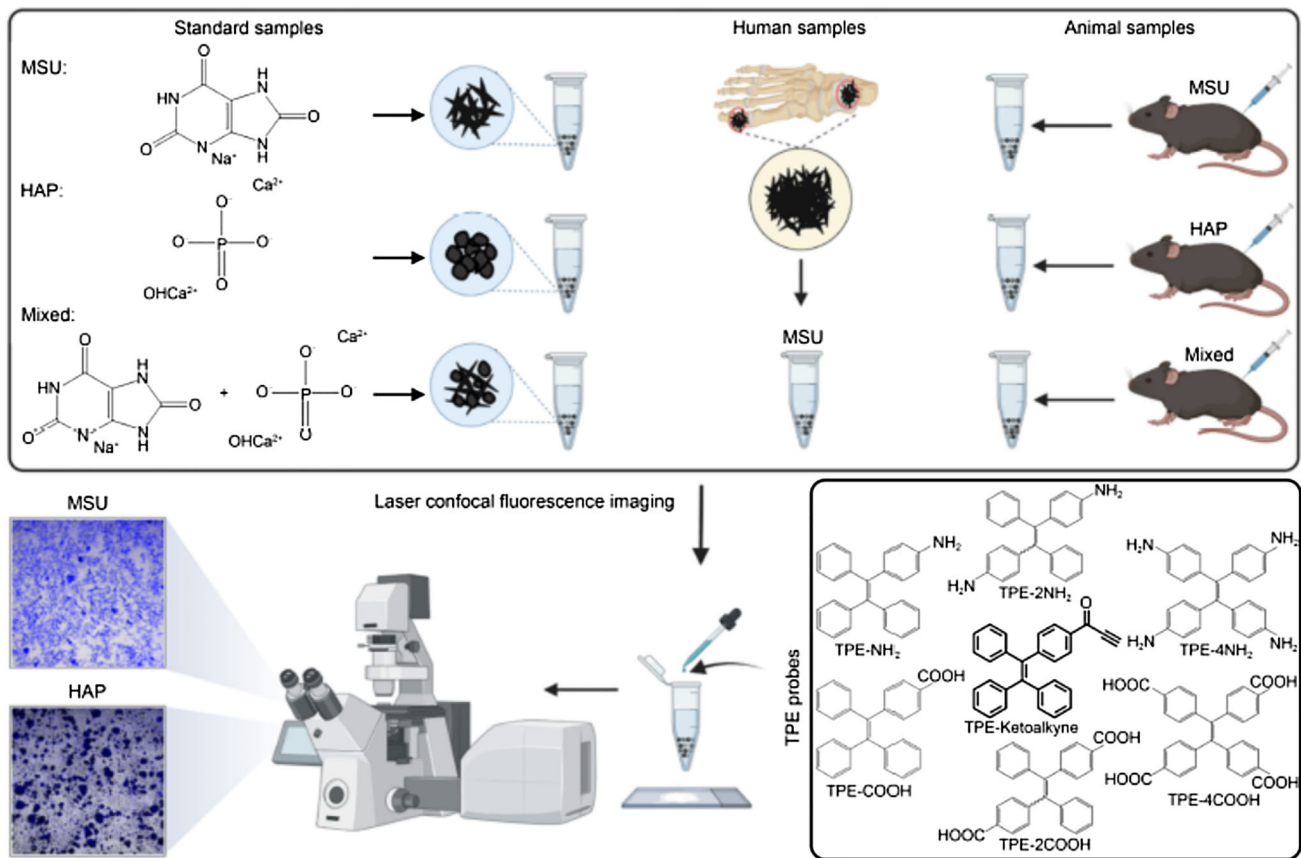
from Molecular Aggregates, South China University of Technology, Guangzhou 510640, China

³ Center for Aggregation-Induced Emission, AIE Institute, South China University of Technology, Guangzhou 510640, China

⁴ School of Chemistry and Chemical Engineering, University of South China, Hengyang 421001, China

⁵ State Key Laboratory of Surface Physics, Department of Physics, Fudan University, Shanghai 200433, China

Graphic abstract



Keywords Gout · Monosodium urate · Hydroxyapatite · TPE-Ketoalkyne · Aggregation-induced emission · Confocal laser scanning microscope imaging

Introduction

Gout is one of the most common forms of inflammatory arthritis and is characterized by the deposition of monosodium urate (MSU) crystals within joints and soft tissues [1]. Over time, repeated deposition of MSU crystals in joints can form a chronic granuloma called a tophus [2], which gradually destroys the joints and thereby causes great pain and inconvenience to sufferers of gout. In addition to joint damage, gout can also increase the risk of cardiovascular and kidney diseases [3, 4]. Other forms of inflammatory arthritis such as basic calcium phosphate crystal arthritis, which is induced by hydroxyapatite (HAP) crystals, can resemble the clinical presentation of gout and need to be differentially diagnosed [5]. At present, the main management strategy for gout is to reduce the MSU crystal deposition via drugs or surgery [1]. Alarmingly, the premature death rate among gout patients has not declined over the past decade, mainly due to misdiagnosis and suboptimal management [6].

Therefore, timely and accurate detection of MSU crystals is critical for the diagnosis and treatment of gout.

Gouty arthritis is most often diagnosed by its clinical presentation combined with the results of several examinations. Traditionally, detection of MSU crystals by compensated polarized light microscope (CPLM) was the gold standard for the diagnosis of gout [7]. However, distinguishing MSU crystals from other crystals (e.g., HAP) solely by CPLM can be challenging, since the assessment process is highly dependent on the proficiency of diagnosticians [8–11]. In recent years, advanced imaging techniques have become available for use in evaluating the diagnostic criteria of gout. These include dual energy computed tomography (DECT), which has relatively high sensitivity and specificity [12, 13]. Nevertheless, DECT also has disadvantages since it uses ionizing radiation and has low sensitivity during the early stages of gout [14–16]. Stimulated Raman scattering microscopy, a relatively new technique that enables high-speed imaging,

has been successful in diagnosing gout using fresh gouty tissues and is able to identify MSU crystals in synovial fluid based on quantitative chemical analyses [17–19]. However, laboratory-grade instruments are bulky and expensive, which are inconvenient for clinical operations. Thus, novel strategies for MSU crystal detection that are both rapid and highly accurate are urgently needed for gout diagnosis and related clinical therapies.

Techniques based on fluorescence have been widely used both in fundamental research and in practical biomedicine, since such assays are noninvasive, highly sensitive, and capable of real-time visualization [20]. However, traditional luminogens can be susceptible to aggregation-caused quenching due to π – π stacking interactions between hydrophobic molecules. This can limit the sensitivity and affect the practicality of clinical applications [21, 22]. Fortunately, fluorophores with aggregation-induced emission (AIE) can use a spontaneous aggregation process to generate bright emissions that are outstandingly sensitive [23, 24]. AIE luminogens (AIEgens) are therefore ideal candidates for biological analysis and imaging applications, including biomolecular detection, cell tracking, and in vivo imaging [25–28]. Moreover, AIEgens have been widely validated, and are known to be stable and highly safe for biomedical applications [29–31], and are therefore an excellent platform for image-guided clinical diagnosis. Thus, the excellent optical performance of AIEgens inspired us to determine which AIEgen would be most suitable for specific, long-term, and rapid imaging of MSU crystals in gouty arthritis in vitro.

In this paper, we consider the unique properties and structures of MSU crystals and identify an effective AIE probe for the selective in vitro imaging of MSU crystals by screening a series of specific probes. The AIE probe identified here can quickly and efficiently label MSU crystals with high sensitivity. Moreover, the process of distinguishing between MSU and HAP crystals may be more convenient and effective using this strategy than the gold standard CPLM method. Furthermore, we were also able to identify MSU crystals from human gouty synovial fluid and tophi. Therefore, we speculate that this AIE-MSU probe may play an important auxiliary role in gout diagnosis, providing a reliable approach for sensitive and long-term rapid detection of MSU crystal-related diseases in clinical settings.

Materials and methods

Materials

Uric acid, sodium hydroxide, 0.1% dilute hydrochloric acid, and HAP crystals were purchased from Aladdin Corporation (China). MSU crystals were obtained using a previously published method involving the pH titration of uric acid [32]. The

RAW264.7 cell line was obtained from the American Type Culture Collection (ATCC; USA). Paraformaldehyde and phosphate buffered saline (PBS), fetal bovine serum, Dulbecco's modified Eagle's medium (DMEM), penicillin, and streptomycin were purchased from Sigma-Aldrich (USA). TRIzol was purchased from Invitrogen (USA). Tetraphenyl ethylene (TPE)-NH₂, TPE-2NH₂, TPE-4NH₂, TPE-COOH, TPE-2COOH, TPE-4COOH, and TPE-Ketoalkyne were synthesized using protocols detailed in previous reports [33–40].

Animal sample collection

The air pouch model was established under an aseptic environment according to a previously published protocol [41, 42]. In brief, eight-week-old male mice were randomly divided into three groups of three mice each. These groups received injections containing MSU crystals, HAP crystals, or a 1:1 (mass ratio) mixture of MSU and HAP crystals. For all injections, 3 mL of filtered air was injected subcutaneously into the back of a mouse to form an air pouch. On day 3, an additional 2 mL of sterile air was injected into the preexisting air pouch. On day 6, 25 mg/mL MSU or HAP crystals or the combined mixture was injected into the air pouch. Mice were sacrificed 24 h after injection and crystal samples were then collected from the air pouches.

Human sample collection

To obtain human specimens, intraoperative synovial fluid or tophus tissue samples were collected from ankle joints ($n=3$) and/or first metatarsophalangeal joints ($n=3$) of gouty patients. All patients had hyperuricemia for more than five years with impaired joint function that met the clinical indications for surgery. Synovial fluid samples were collected and diluted in a centrifuge tube containing PBS and were filtered to obtain MSU crystals. In addition, tophus specimens were placed in a centrifuge tube containing PBS to separate MSU crystals from the tissue. Large, visible portions of tissue were removed and the remaining liquid was centrifuged at 1000 r/min. The supernatant was then discarded and the MSU crystals were collected. All collected MSU crystals were then filtered and oven-dried. Finally, the dried MSU crystals were stored in sterile centrifuge tubes for subsequent experiments.

Imaging instruments

MSU or HAP crystals or a mixture of both was identified using a CPLM manufactured by Olympus (Japan) and a confocal laser scanning microscope (CLSM) from Nikon (Japan). The excitation wavelength was set to 405 nm for CLSM imaging of all samples. A Shimadzu UV-2600 spectrophotometer was used to measure the ultraviolet–visible (UV–Vis) absorption spectra. Photoluminescence spectra

were recorded using a Horiba Fluoromax-4 spectrofluorometer (HORIBA, Japan). Luminescence of MSU crystal solutions was quantified using 395 nm laser irradiation.

Cell culture

The RAW264.7 cell line was cultured in DMEM supplemented with 10% fetal bovine serum at 37 °C in 5% CO₂. The cell line was then used for subsequent experiments. A mixture of MSU crystals and TPE-Ketoalkyne was added to cells incubated in confocal dishes. The final concentration of TPE-Ketoalkyne was 40 μmol/L. After 30 min, the upper culture medium was then discarded before CLSM imaging.

Cell counting kit-8 (CCK-8) assays

The viability of RAW264.7 cells treated with TPE-Ketoalkyne was examined using a CCK-8 activity assay kit (Abcam, UK). Briefly, cells were placed in 96-well plates and then treated with TPE-Ketoalkyne at different concentrations ranging from 5 to 80 μmol/L. After treatment with an AIE probe, the cells were cultured at 37 °C with 5% CO₂ for 48 h. The absorbance at 450 nm was then measured on a microplate reader (Thermo Fisher Scientific, USA).

Quantitative real-time polymerase chain reaction (qRT-PCR)

For qRT-PCR, total RNA was first extracted using TRIzol from a RAW264.7 cell line treated with TPE-Ketoalkyne. The RNA was then reverse transcribed into cDNA using a RevertAid First Strand cDNA Synthesis Kit (Thermo Scientific, USA). qRT-PCR was then performed using a SYBR Green PCR master mix (Toyobo, Japan) with all procedures performed according to the manufacturer's instructions. The primers used were as follows: mouse interleukin-1β (*IL-1β*) (forward 5'-TGCCACCTTTTGACAGTGATG-3' and reverse 5'-CATCTCGGAGCCTGTAGTGC-3'), and mouse tumor necrosis factor-α (*TNF-α*) (forward 5'-TGGAAGTGGCAGAAGAGGCAC-3' and reverse 5'-AGGGTCTGGGCCATAGAACTGA-3'). The relative expression of *IL-1β* and *TNF-α* was then analyzed by the 2^{-ΔΔCt} method to compare between groups. All experiments were performed using three technical replicates.

TdT-mediated dUTP nick-end labeling (TUNEL) assays

Apoptosis in RAW264.7 cells treated with TPE-Ketoalkyne was assessed using a TUNEL Assay Kit-fluorescein isothiocyanate (FITC) (Abcam, UK). Briefly, cells were treated with TPE-Ketoalkyne at different concentrations ranging from 5 to 80 μmol/L, and then cultured at 37 °C with 5% CO₂ for

48 h. Treated cells were then collected, washed with PBS, and fixed in 4% paraformaldehyde for 15 min. Thereafter, fixed cells were incubated with a staining solution at room temperature for 1 h. Subsequently, cell samples were stained with FITC (Invitrogen, USA). Finally, CLSM was used to image and estimate the percentage of apoptotic cells.

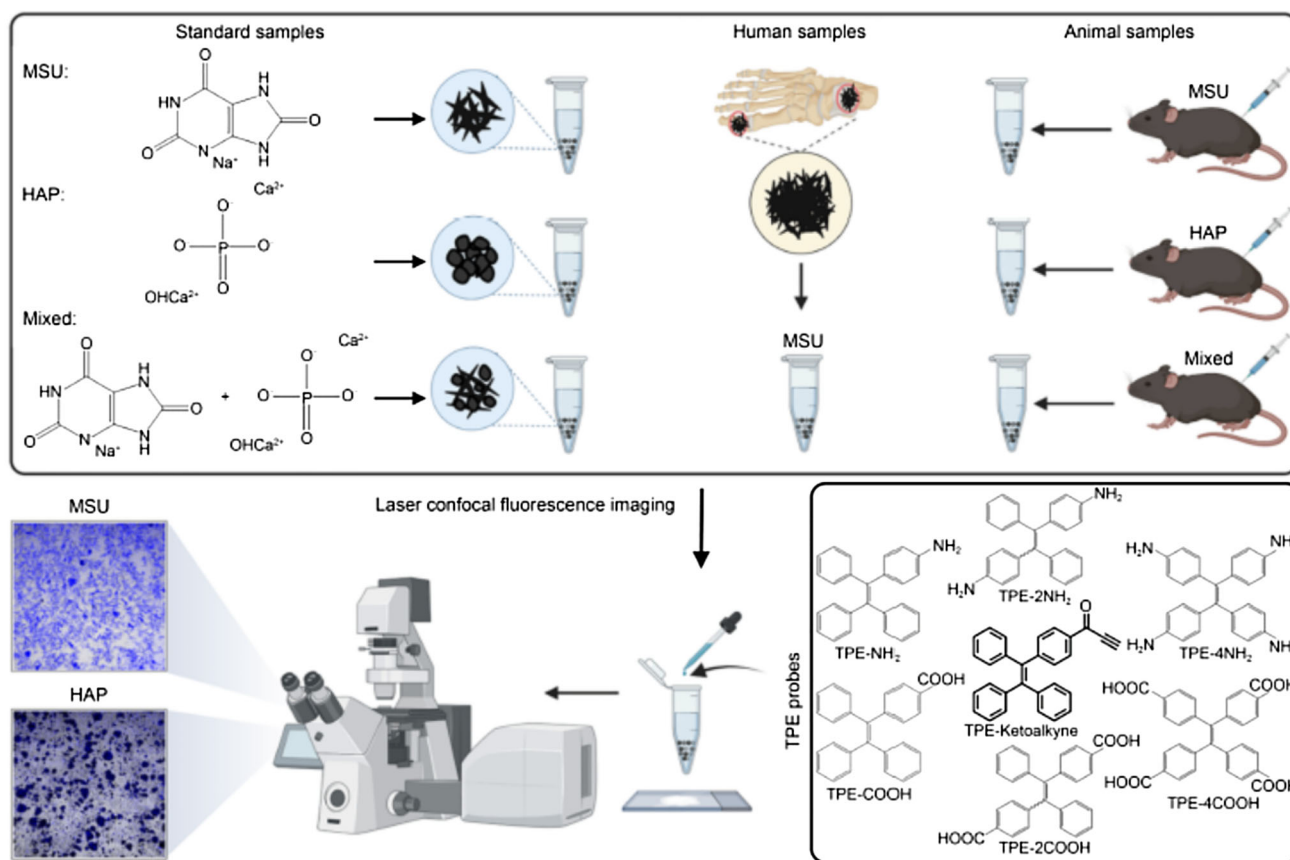
Statistical analyses

ImageJ was used for quantitative analysis of all images. Statistical analyses were performed using GraphPad Prism version 8.0.1. Data were tested for normality before *t*-tests were used to assess the statistical significance of differences between group means. Data were presented as the mean ± standard deviation of three independent experiments (**p*<0.05, ***p*<0.01, ****p*<0.001).

Results

Photophysical properties of luminogens

As illustrated in Scheme 1, MSU crystals were generated from uric acid, which is poorly soluble in water. Seven TPE-containing luminogens (i.e., TPE-NH₂, TPE-2NH₂, TPE-4NH₂, TPE-COOH, TPE-2COOH, TPE-4COOH, and TPE-Ketoalkyne) that possess different charge and hydrophobicity characteristics were selected to investigate the efficiency of their binding with MSU crystals. By systematically exploring the optical properties of these luminogens in the absence and presence of MSU/HAP crystals, we identified TPE-Ketoalkyne as the optimal luminogen, since it showed both high selectivity and sensitivity toward MSU crystals. First, we examined the photophysical properties of these luminogens in detail. As shown in Fig. 1a, the absorptions of all luminogens ranged from 300 to 440 nm. We hypothesized that the maximum absorption would indicate a bathochromic-shift from enhanced donor–acceptor structures. Taking amino group-modified TPE as an example, with an increased number of amino groups, TPE derivatives showed an obvious bathochromic-shift from 334 to 352 nm. For example, TPE-Ketoalkyne presented a maximum absorption of 353 nm since it possesses a novel carbonyl group. A similar trend in fluorescence emission was also observed for the AIEgens (Fig. 1b). Photoluminescence (PL) spectra indicated that TPE-Ketoalkyne showed bright green fluorescence with a maximum emission at 503 nm. Moreover, the AIE behavior of these luminogens was further studied by measuring their PL intensity when present in H₂O/tetrahydrofuran (THF) mixtures of different water fractions. We found that compared to other luminogens, TPE-Ketoalkyne showed the highest fluorescence emissions when the water fraction



Scheme 1 Schematic illustration of fluorescently labeled MSU crystals in gouty arthritis. MSU: monosodium urate; HAP: hydroxyapatite

was above 90% (Figs. 1c–1i). This indicated that TPE-Ketoalkyne became highly emissive in an aggregate state, which is a characteristic behavior of AIEgens, and is therefore promising for high-sensitivity detection and analytic applications.

AIE-MSU probe optimization

To identify the optimal probe for MSU detection and imaging, we isolated specific probes and separately mixed them with MSU crystals before observation using CLSM imaging. As shown in Fig. 2a, for luminogens with amino groups (i.e., TPE-NH₂, TPE-2NH₂, and TPE-4NH₂), we observed no obvious aggregated fluorescence on MSU crystals that were randomly distributed in the solutions; this demonstrated that these probes cannot effectively bind to the MSU crystals. These results showed that positively charged amino groups were not ideal for labeling MSU crystals. However, unlike amino group-bearing luminogens, strong fluorescence was detected on MSU crystals treated with probes containing carboxyl groups (i.e., TPE-COOH, TPE-2COOH, and TPE-4COOH). Nevertheless, this fluorescent signal decreased strongly with the increasing number of carboxyl groups present on the probe (Fig. 2b), indicating that enhanced

hydrophilicity would reduce their binding toward the crystals. Furthermore, bright fluorescence was observed on MSU crystals mixed with TPE-Ketoalkyne (Fig. 2c), indicating that this probe efficiently bound to MSU crystals. To exclude the possibility of cluster luminescence of MSU crystals, we observed the fluorescence intensity of MSU crystals both in the absence and presence of TPE-Ketoalkyne. These results verified that bright fluorescence was only detected on MSU crystals in the presence of TPE-Ketoalkyne (Figs. S1a–S1c in Supplementary Information), thereby proving that there existed no cluster luminescence of MSU crystals. After further calculating and comparing of fluorescence intensities among different samples, TPE-Ketoalkyne was identified as the most desirable probe for high-sensitivity MSU crystal labeling and detection (Fig. 2d). Combining these results, we conclude that the appropriate hydrophobicity of the probe is critical for the realization of MSU crystal binding and detection.

Binding behavior observation

To further evaluate the ability of TPE-Ketoalkyne to detect MSU crystals, we then systematically investigated its binding

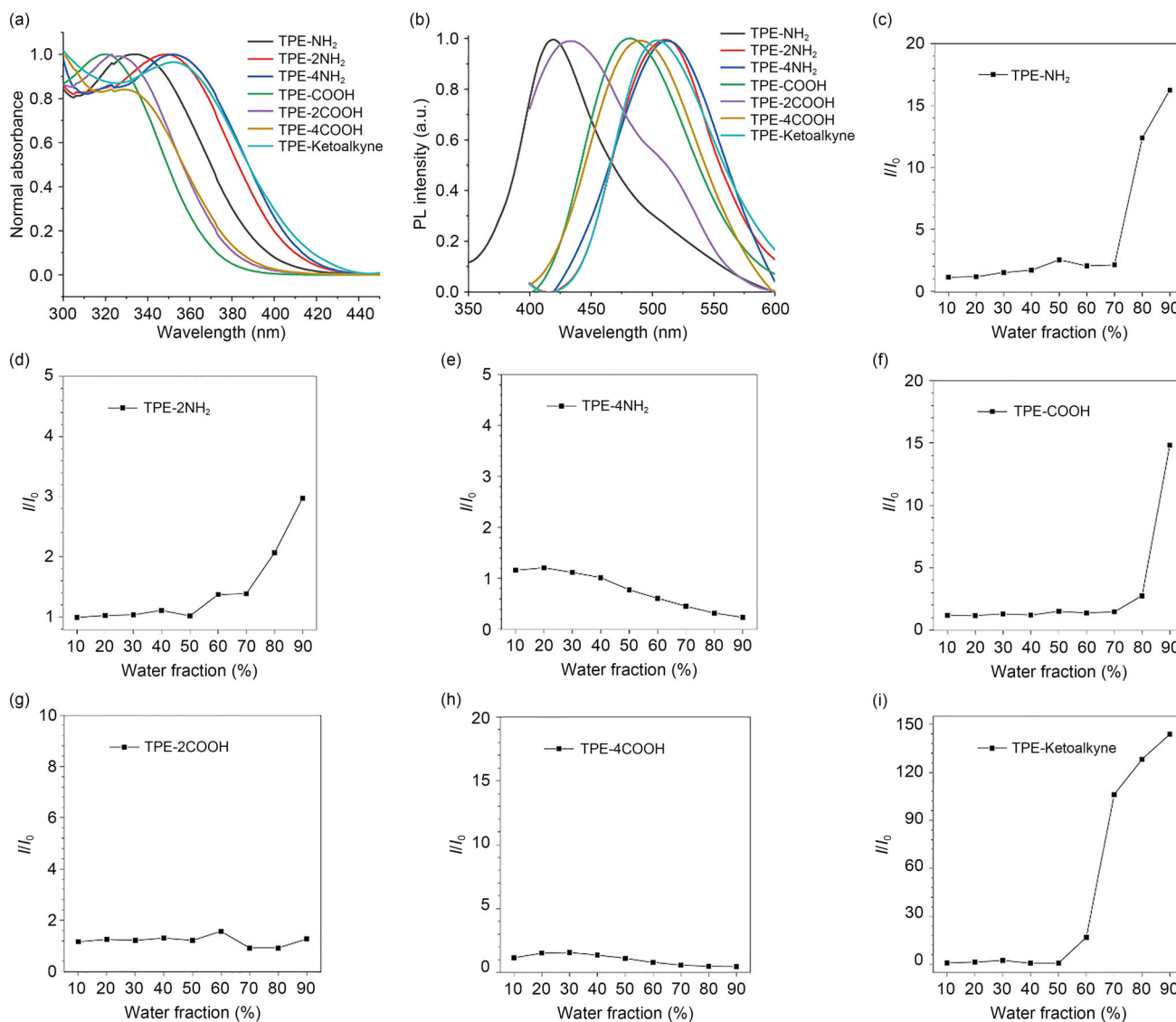


Fig. 1 Optical spectra of different luminogens. **a** Normalized absorption spectra of TPE-NH₂, TPE-2NH₂, TPE-4NH₂, TPE-COOH, TPE-2COOH, TPE-4COOH, and TPE-Ketoalkyne (10 μmol/L). **b** PL spectra of seven TPE probes (10 μmol/L) in THF. **c–i** Relative emis-

sion intensity (I/I_0) of each of the TPE probes (10 μmol/L) in THF/H₂O mixtures with varying water fractions. TPE: tetraphenyl ethylene; PL: photoluminescence; THF: tetrahydrofuran

behavior. To do so, we monitored the fluorescence intensity in samples where the concentration of TPE-Ketoalkyne ranged from 5 to 80 μmol/L. As shown in Fig. 3a, fluorescence intensity strongly increased at higher concentrations of TPE-Ketoalkyne. By optimizing the reactant concentration in sequence, 10 μmol/L of TPE-Ketoalkyne was considered to be the minimum concentration for efficient MSU crystal labeling (Fig. 3b). Moreover, three-dimensional (3D) constructions of MSU crystals based on fluorescence imaging revealed the desirable imaging behavior of TPE-Ketoalkyne toward MSU crystals (Fig. 3c). In addition, with increasing incubation time, the fluorescence intensity of both the MSU

crystal suspension and the dried MSU crystals labeled by TPE-Ketoalkyne gradually enhanced. This dynamic process was visualized and recorded on video (Videos 1 and 2 in Supplementary Information).

MSU and HAP crystals

The discrimination between MSU and HAP crystals is important in clinical settings, but this is not easy since these crystals appear to be highly similar. We therefore compared the binding behavior of TPE-Ketoalkyne toward both MSU and HAP crystals under the same conditions. As shown in Fig. 4a,

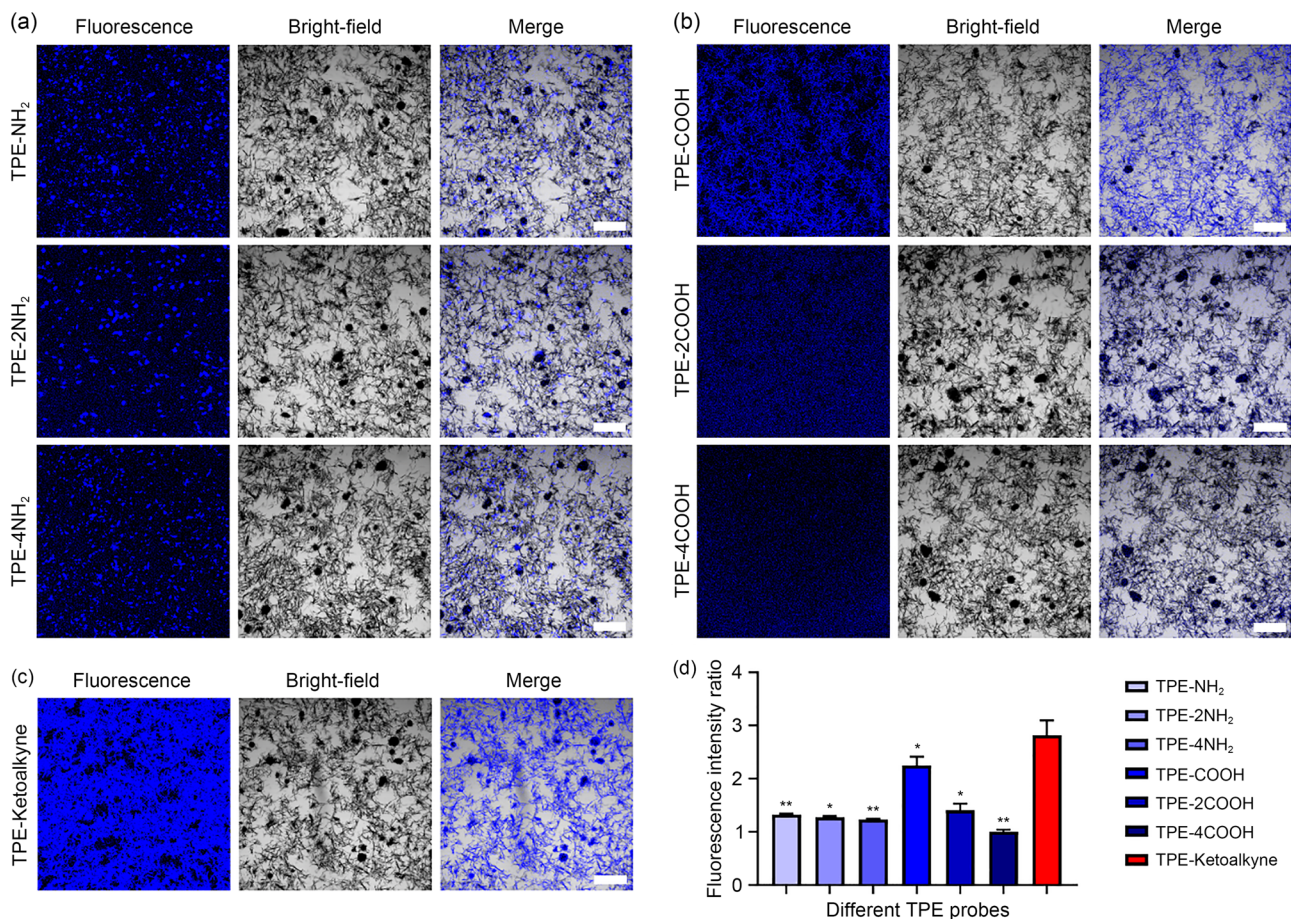


Fig. 2 Luminogens for MSU crystal labeling. **a** CLSM images of MSU crystals mixed with TPE-NH₂, TPE-2NH₂, and TPE-4NH₂, respectively. **b** CLSM images of MSU crystals mixed with TPE-COOH, TPE-2COOH, and TPE-4COOH, respectively. **c** CLSM images of MSU crystals mixed with TPE-Ketoalkyne. Concentration of MSU crystal solution: 50 mg/mL; molecular concentration of all TPE solutions:

80 μmol/L; excitation wavelength: 405 nm; scale bar: 200 μm. **d** Quantitative analysis of the relative fluorescence intensity of MSU crystals mixed with each luminogen. **p*<0.05, ***p*<0.01. MSU: monosodium urate; CLSM: confocal laser scanning microscope; TPE: tetraphenyl ethylene

the fluorescence intensity of MSU groups was much greater than the HAP groups. Moreover, the fluorescent signals of the MSU groups were distributed on the crystals, while only a random fluorescent signal could be observed around HAP crystals. Furthermore, even in the mixed sample, the bright fluorescent signal was detected only on MSU crystals (Fig. 4b), demonstrating the high selectivity and sensitivity of TPE-Ketoalkyne toward MSU crystals. Meanwhile, CPLM, the gold standard for MSU crystal detection, was performed under the same conditions without TPE-Ketoalkyne. As shown in Fig. 4c, when MSU crystals were present alone, detection via CPLM was easy, but this technique exhibited poor imaging accuracy for HAP crystals. In the mixed crystal sample, CPLM could not specifically and conveniently distinguish MSU from HAP crystals (Fig. 4c). Therefore, our results showed that TPE-Ketoalkyne was superior to CPLM for distinguishing between MSU and HAP crystals. We also noted that the detection of MSU crystals using

AIE technology did not require professional operation and was not subject to subjective identification under the microscope; the existence of MSU crystals can be confirmed by AIE alone. Therefore, we concluded that high-sensitivity and highly-specific imaging of MSU crystals was realized using TPE-Ketoalkyne. This could potentially reduce artifactual false positives and false negatives efficiently.

To further verify the selectivity of TPE-Ketoalkyne, we examined its binding behavior with MSU and HAP crystals in mouse air pouch models. As shown in Fig. S2 (Supplementary Information), we observed highly selective behavior, which further demonstrated the advantages of AIE probes for MSU crystal detection.

Biocompatibility evaluation

Since macrophages play a critical role in activation of the nucleotide oligomerization domain (NOD)-like receptor thermal protein domain associated protein 3 (NLRP3)

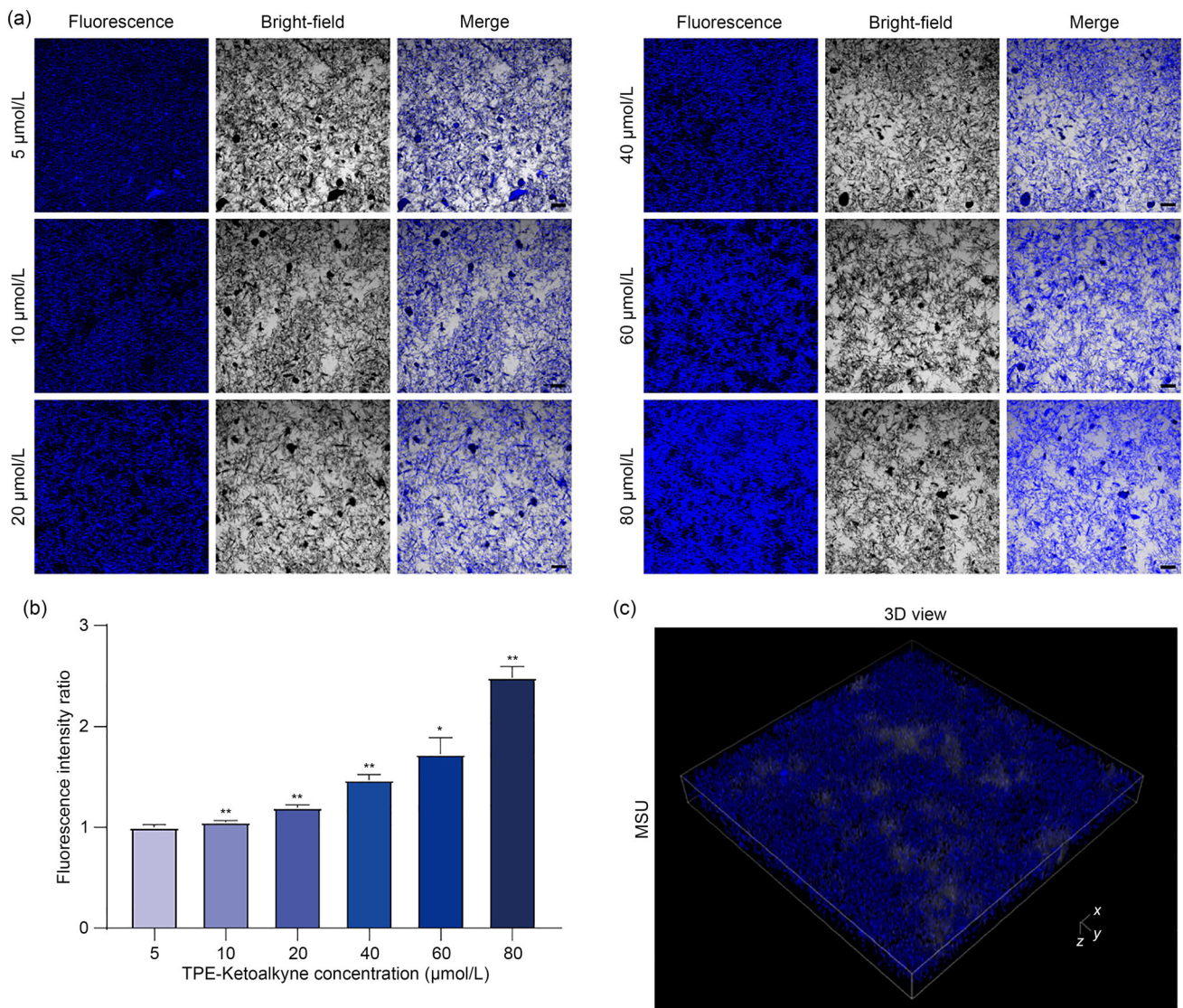


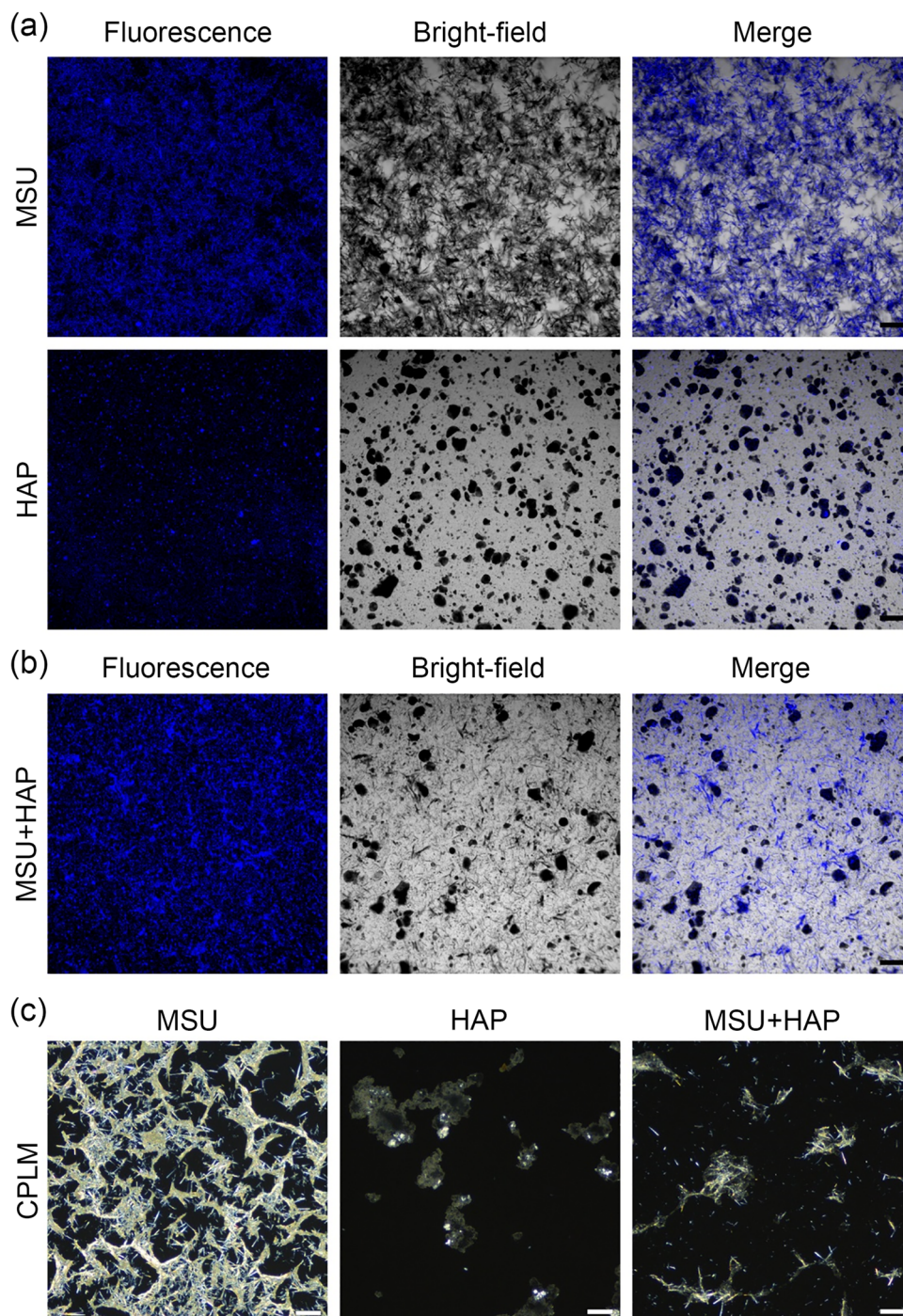
Fig. 3 Imaging of TPE-Ketoalkyne with MSU crystals. **a** CLSM images of 50 mg/mL MSU crystals mixed with TPE-Ketoalkyne at concentrations ranging from 5 to 80 $\mu\text{mol/L}$. Excitation wavelength: 405 nm; scale bar: 100 μm . **b** Quantitative analysis of the relative fluorescence intensity of 50 mg/mL MSU crystal solutions mixed with TPE-Ketoalkyne at concentrations ranging from 5 to 80 $\mu\text{mol/L}$. * $p < 0.05$,

** $p < 0.01$. **c** CLSM 3D image of 50 mg/mL MSU crystals mixed with 10 $\mu\text{mol/L}$ TPE-Ketoalkyne. Excitation wavelength: 405 nm. Calibration x: 1.24 μm ; y: 1.24 μm ; z: 15.00 μm . Width: 1272.79 μm ; height: 1272.79 μm ; depth: 135.00 μm . TPE: tetraphenyl ethylene; MSU: monosodium urate; CLSM: confocal laser scanning microscope

inflammasome in gout, TPE-Ketoalkyne was then employed to monitor the in vitro phagocytosis of MSU crystals by the murine macrophage cell line RAW264.7. As shown in Fig. 5a, MSU crystals in RAW264.7 cells were brightly fluorescent, which further confirms the sensitivity and selectivity of TPE-Ketoalkyne. In addition, we noted that probe biosafety is a critical parameter for biomedical applications, so we further evaluated the biocompatibility of TPE-Ketoalkyne. First, we studied the expression of mRNAs related to inflammatory factors, including *IL-1 β* and *TNF- α* . As shown in Figs. 5b and 5c, mRNA expression levels changed slightly when the concentration of TPE-Ketoalkyne

was less than 40 $\mu\text{mol/L}$. This indicated that such a low concentration of the AIE probe had little effect on the inflammatory activation of RAW264.7 cells. To further investigate the cytotoxicity, we incubated RAW264.7 cells with different concentrations of TPE-Ketoalkyne and conducted CCK-8 assays. The results demonstrated that cell viabilities remained above 90% after treatment with 40 $\mu\text{mol/L}$ of TPE-Ketoalkyne, indicating low cytotoxicity and good biocompatibility of the probe (Fig. 5d). Moreover, TUNEL staining results indicated that a faint apoptosis signal of the RAW264.7 cell could be detected after treatment with TPE-Ketoalkyne (Figs. 5e and 5f). Taken together, these results

Fig. 4 Specific imaging of TPE-Ketoalkyne for differential diagnosis of MSU and HAP crystals. **a** CLSM images of 50 mg/mL MSU and HAP crystals mixed with 10 $\mu\text{mol/L}$ TPE-Ketoalkyne, respectively. Excitation wavelength: 405 nm; scale bar: 100 μm . **b** CLSM images of a mixture of equal proportions of MSU and HAP crystals mixed with 40 $\mu\text{mol/L}$ TPE-Ketoalkyne. Excitation wavelength: 405 nm; scale bar: 100 μm . **c** CPLM images of MSU crystals, HAP crystals, and a mixture of equal proportions of MSU and HAP crystals. Scale bar: 100 μm . TPE: tetraphenyl ethylene; MSU: monosodium urate; HAP: hydroxyapatite; CLSM: confocal laser scanning microscope; CPLM: compensated polarized light microscope



verified the outstanding biosafety of TPE-Ketoalkyne for bioimaging applications.

Clinical application exploration

Thus far, we have demonstrated the high selectivity and sensitivity of TPE-Ketoalkyne for the labeling of MSU crystals. Next, we tested the diagnostic ability of TPE-Ketoalkyne using clinical samples such as human synovial fluid and

tophi. In these clinical samples, high detection efficiency toward MSU crystals was acquired using 10 $\mu\text{mol/L}$ of TPE-Ketoalkyne, which was comparable to CPLM characterization (Figs. 6a–6d). Then, we conducted time series imaging to observe the speed of the probe during aggregation-induced luminescence after binding to MSU crystals from gouty tophi (Video 3 in Supplementary Information). The results showed that TPE-Ketoalkyne could effectively detect MSU crystals within one minute (Fig. 6e). Simultaneously, a

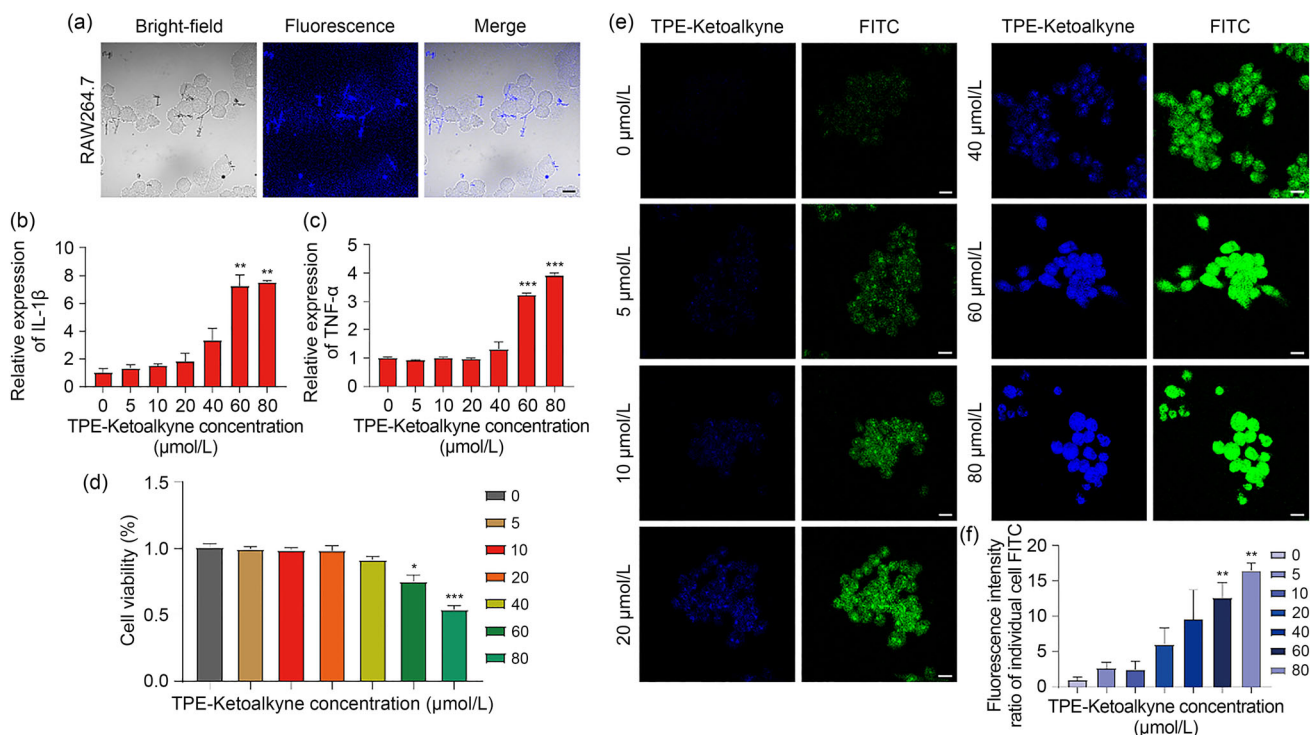


Fig. 5 Application of TPE-Ketoalkyne for intracellular MSU crystal imaging. **a** CLSM images of MSU crystals in RAW264.7 cells with 10 $\mu\text{mol/L}$ TPE-Ketoalkyne. Excitation wavelength: 405 nm; scale bar: 10 μm . **b**, **c** The relative mRNA expression levels of *IL-1 β* and *TNF- α* in RAW264.7 cells at TPE-Ketoalkyne concentrations ranging from 5 to 80 $\mu\text{mol/L}$ after 48 h. **d** CCK-8 cytotoxicity assays of RAW264.7 cells at different TPE-Ketoalkyne concentrations ranging from 5 to 80 $\mu\text{mol/L}$ after 48 h. **e** TUNEL apoptosis assays of RAW264.7 cells at TPE-Ketoalkyne concentrations ranging from 5 to

80 $\mu\text{mol/L}$ after 48 h. Blue stain: TPE-Ketoalkyne; excitation wavelength: 405 nm. Green stain: FITC; excitation wavelength: 490 nm. Scale bar: 10 μm . **f** Quantification of the relative fluorescence intensity of FITC at TPE-Ketoalkyne concentrations ranging from 5 to 80 $\mu\text{mol/L}$ after 48 h. * $p < 0.05$, ** $p < 0.01$, *** $p < 0.001$. TPE: tetraphenyl ethylene; MSU: monosodium urate; CLSM: confocal laser scanning microscope; TUNEL: TdT-mediated dUTP nick-end labeling; FITC: fluorescein isothiocyanate

3D visualization of MSU crystals based on fluorescent imaging showed a high overlap between TPE-Ketoalkyne and MSU crystals from gouty tophi (Fig. 6f). Taken together, these data confirmed that TPE-Ketoalkyne can rapidly and effectively detect MSU crystals from samples taken from gouty patients. Thus, we speculated that TPE-Ketoalkyne shows considerable promise for clinical diagnostic applications.

Discussion

Various imaging techniques for gout diagnosis and treatment have been developed. However, clinical diagnosis strategies that use these techniques possess significant disadvantages, such as damage from exposure to ionizing radiation (for DECT), and the high level of professional training required (for CPLM detection). This work provides a novel and reliable method for the detection and diagnosis of gout.

Due to their high sensitivity and biosafety, AIE-based technologies are playing an increasingly important role in

biomedical imaging in both in vivo and in vitro analyses. Based on the well-defined AIE mechanism, here we have optimized desirable AIE probes for MSU crystal detection and labeling for the first time. To reveal the mechanism responsible for probe labeling, we investigated the binding behavior between TPE-Ketoalkyne and MSU crystals. Due to the high reactivity of yne groups, we first examined the presence of covalent binding between the two agents. However, after using nuclear magnetic resonance, infrared spectra, and high resolution mass spectrum, we did not detect covalent binding between TPE-Ketoalkyne and MSU crystals, thereby demonstrating that this binding must be noncovalent. We then systematically studied the relationship between the probe hydrophobicity and fluorescence intensity when bound to MSU crystals. Owing to the presence of amino and carboxyl groups, TPE-NH₂, TPE-2NH₂, TPE-4NH₂, TPE-COOH, TPE-2COOH, and TPE-4COOH possess different degrees of hydrophilicity. However, TPE-Ketoalkyne has relatively high hydrophobicity, with a hydrophobic coefficient

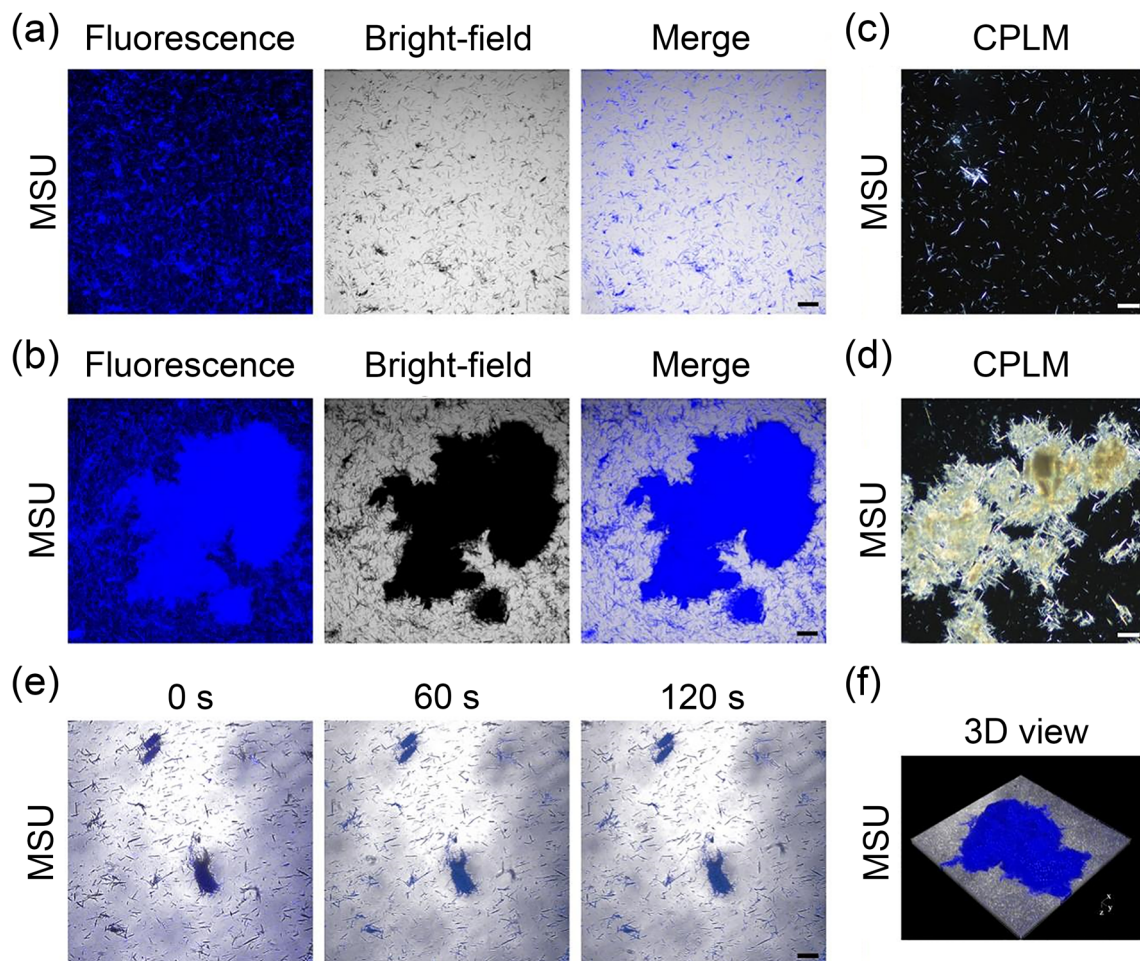


Fig. 6 Imaging behavior for clinical applications. **a** CLSM images of MSU crystals sourced from human gouty synovial fluid after mixing with 10 $\mu\text{mol/L}$ TPE-Ketoalkyne. Excitation wavelength: 405 nm; scale bar: 100 μm . **b** CLSM images of MSU crystals sourced from human tophi of gout mixed with 10 $\mu\text{mol/L}$ TPE-Ketoalkyne. Excitation wavelength: 405 nm; scale bar: 100 μm . **c** CPLM image of MSU crystals sourced from human gouty synovial fluid. Scale bar: 100 μm . **d** CPLM image of MSU crystals sourced from human tophi of gout. Scale bar: 100 μm . **e** CLSM time series images of MSU crystals sourced from

human tophi of gout mixed with 10 $\mu\text{mol/L}$ TPE-Ketoalkyne. Excitation wavelength: 405 nm; scale bar: 100 μm . **f** CLSM 3D image of MSU crystals sourced from human tophi of gout mixed with 10 $\mu\text{mol/L}$ TPE-Ketoalkyne. Excitation wavelength: 405 nm. Calibration x : 1.24 μm ; y : 1.24 μm ; z : 10.00 μm . Width: 1272.79 μm ; height: 1272.79 μm ; depth: 50.00 μm . CLSM: confocal laser scanning microscope; MSU: monosodium urate; TPE: tetraphenyl ethylene; CPLM: compensated polarized light microscope

of 6.52. Given these results, we speculated that the hydrophobic interactions between TPE-Ketoalkyne and MSU crystals were a critical determinant of the specific imaging of MSU crystals.

More importantly, we found that the highly sensitive TPE-Ketoalkyne labeling method reported here was comparable to CPLM characterization during examination of many different kinds of MSU crystal samples, including standard samples, samples from mouse models of acute gout, and clinical samples. Unlike the CPLM method, no professional operation or subjective assessment is required for AIE-MSU probe characterization. In addition, the easy operation and high biosafety of this approach were repeatedly demonstrated and verified. Therefore, we conclude that this protocol is ideal

for high-sensitivity diagnostics and may have broad applications in clinical settings.

HAP crystal deposition diseases often involve the metacarpophalangeal and proximal interphalangeal joints [43, 44], and are therefore similar to cases in which gout attacks facet joints. Of particular concern is that HAP crystal deposition diseases are associated with soft tissue inflammation and edema during the acute inflammatory phase, and this may be misdiagnosed as gout [45]. Although the prevalence of HAP crystal deposition diseases is not as high as that of gout, clinicians must still make an accurate differential diagnosis when patients present with HAP or MSU crystal deposition diseases. Moreover, previous studies could not effectively distinguish between MSU and HAP crystals.

For example, Park et al. described the potential of optical diffraction tomography in the diagnosis of gout, but this approach cannot distinguish between MSU crystals and other types of crystals [46]. In addition, studies have shown the potential of spectral photon-counting radiography for the detection of MSU and HAP crystals [47], but this instrument is laboratory-scale and quite bulky. Moreover, it requires professional operation and increases the time cost of outpatient diagnosis. In this study, we identified TPE-Ketoalkyne as an excellent probe for distinguishing between MSU and HAP crystals. Moreover, the use of AIE-MSU probe technology can accurately and rapidly distinguish between these two crystal deposition diseases in outpatient clinics, and can therefore help patients avoid missing the best treatment period due to misdiagnosis.

In this study, we demonstrated that TPE-Ketoalkyne facilitated specific fluorescence imaging of MSU crystals *in vitro*, and was especially capable of distinguishing MSU from HAP crystals. The operation is cost effective and simple, and therefore this protocol has significant promise as a standard approach for diagnosis. Given its easy operation and high sensitivity, this method could be employed to characterize the samples extracted from patients' joints with high efficiency for both outpatient and inpatient departments. Notably, MSU crystals could be monitored over long periods since the AIE-MSU probe is nonquenchable. Therefore, this approach may also be eligible for screening or follow-up visits of patients with an MSU crystal-associated arthropathy. Furthermore, this technique may play a role in the assessment of preclinical or asymptomatic patients in the future, and may therefore contribute to preventive screening for gout and related diseases.

In addition to the advantages, we also noted some limitations of the probe-based strategy identified here. For example, due to the poor penetration ability of TPE-Ketoalkyne with respect to the joint cavity, this strategy can only be used for *in vitro* detection. Besides, the selective binding ability of AIE probes to MSU crystals may be further improved to enhance their sensitivity. Given these limitations, we identified possible avenues of future research. First, AIE imaging inspired us to increase the fluorescence wavelength to realize *in vivo* imaging, which is beneficial for noninvasive diagnosis. It can enable the real-time specific imaging of the MSU crystal formation process and permit accurate detection of the 3D spatial and temporal distribution of crystals *in vivo*. Moreover, it may also be possible to further optimize the structures of AIE-MSU probes to improve their specificity toward different crystals, or to further reduce their biotoxicity for *in vivo* imaging. In the future, combining AIE probe fluorescence imaging with other auxiliary imaging technologies for multimodal imaging may also permit the diagnosis and evaluation of gout on multiple levels.

Conclusions

In summary, based on systematical optimization, we have demonstrated for the first time that the specific labeling and imaging of MSU crystals in both standard and clinical samples can be achieved with high selectivity and sensitivity by TPE-Ketoalkyne. This strategy was capable of the detection and discrimination of MSU crystals from HAP crystals and may therefore reduce errors associated with subjective judgment. This work is expected to facilitate development of a noninvasive, simple, and safe strategy for the auxiliary diagnosis and treatment of gout and other MSU crystal-related diseases in the future.

Supplementary Information The online version contains supplementary material available at <https://doi.org/10.1007/s42242-023-00252-4>.

Acknowledgements This work was supported by the Shanghai Science and Technology Committee (No. 22dz1204700), the National Key R&D Program of China (Nos. 2020YFA0803800 and 2017YFE0132200), the National Natural Science Foundation of China (Nos. 82072510, 21907034, 21788102, 21525417, and 51620105009), the Natural Science Foundation of Guangdong Province (Nos. 2019B030301003 and 2016A030312002) and the Innovation and Technology Commission of Hong Kong (No. ITC-CNERC14S01).

Author contributions WJW and RH designed the study. WJW, GQZ, ZYC, and BHZ participated in all the experiments. WJW, GQZ, and HLX performed the data analyses. WJW and GQZ wrote and revised the manuscript. RH, AJQ, and YHH supervised the entire study process.

Declarations

Conflict of interest The authors declare that they have no conflict of interest.

Ethical approval All experiments involving mice were approved by the Animal Welfare and Ethics Group of the Department of Experimental Animal Science, Shanghai Medical College of Fudan University (Shanghai, China; Ethics Approval No. 2019020405). All experiments involving human specimen collection were approved by the Ethics Committee of Huashan Hospital (Shanghai, China; Ethics Approval No. KY2020-060).

References

1. Dalbeth N, Gosling AL, Gaffo A et al (2021) Gout. *Lancet* 397(10287):1843–1855. [https://doi.org/10.1016/S0140-6736\(21\)00569-9](https://doi.org/10.1016/S0140-6736(21)00569-9)
2. Sapsford M, Gamble GD, Aati O et al (2017) Relationship of bone erosion with the urate and soft tissue components of the tophus in gout: a dual energy computed tomography study. *Rheumatology* 56(1):129–133. <https://doi.org/10.1093/rheumatology/kew383>
3. Stamp LK, Farquhar H, Pisaniello HL et al (2021) Management of gout in chronic kidney disease: a G-CAN consensus statement on the research priorities. *Nat Rev Rheumatol* 17(10):633–641. <https://doi.org/10.1038/s41584-021-00657-4>
4. Choi HK, McCormick N, Yokose C (2022) Excess comorbidities in gout: the causal paradigm and pleiotropic approaches to

- care. *Nat Rev Rheumatol* 18(2):97–111. <https://doi.org/10.1038/s41584-021-00725-9>
5. Dalbeth N, Merriman TR, Stamp LK (2016) Gout. *Lancet* 388(10055):2039–2052. [https://doi.org/10.1016/S0140-6736\(16\)00346-9](https://doi.org/10.1016/S0140-6736(16)00346-9)
 6. Richette P, Doherty M, Pascual E et al (2020) 2018 updated European League Against Rheumatism evidence-based recommendations for the diagnosis of gout. *Ann Rheum Dis* 79(1):31–38. <https://doi.org/10.1136/ANNRHEUMDIS-2019-215315>
 7. Nhi LHH, Minh LHN, Tieu TM et al (2021) Role of dual-energy computed tomography in the identification of monosodium urate deposition in gout patients: a comprehensive analysis of 828 joints according to structural joint damage. *Cureus* 13(11):e19930. <https://doi.org/10.7759/cureus.19930>
 8. Schumacher HR, Sieck MS, Rothfuss S et al (1986) Reproducibility of synovial fluid analyses. A study among four laboratories. *Arthritis Rheum* 29(6):770–774. <https://doi.org/10.1002/art.1780290610>
 9. Gordon C, Swan A, Dieppe P (1989) Detection of crystals in synovial fluids by light microscopy: sensitivity and reliability. *Ann Rheum Dis* 48(9):737–742. <https://doi.org/10.1136/ard.48.9.737>
 10. Park JW, Ko DJ, Yoo JJ et al (2014) Clinical factors and treatment outcomes associated with failure in the detection of urate crystal in patients with acute gouty arthritis. *Korean J Intern Med* 29(3):361–369. <https://doi.org/10.3904/kjim.2014.29.3.361>
 11. Anugu A, Monastero R, Pentylala S et al (2021) Clinical validation of rapid gout detection method and kit. *Methods Protoc* 4(4):69. <https://doi.org/10.3390/mps4040069>
 12. Li SS, Xu GH, Liang JY et al (2021) The role of advanced imaging in gout management. *Front Immunol* 12:811323. <https://doi.org/10.3389/fimmu.2021.811323>
 13. Stewart S, Su I, Gamble GD et al (2021) Diagnostic value of different imaging features for patients with suspected gout: a network meta-analysis. *Semin Arthritis Rheum* 51(6):1251–1257. <https://doi.org/10.1016/j.semarthrit.2021.10.005>
 14. Gamala M, Jacobs JWG, van Laar JM (2019) The diagnostic performance of dual energy CT for diagnosing gout: a systematic literature review and meta-analysis. *Rheumatology* 58(12):2117–2121. <https://doi.org/10.1093/rheumatology/kez180>
 15. Bongartz T, Glazebrook KN, Kavros SJ et al (2015) Dual-energy CT for the diagnosis of gout: an accuracy and diagnostic yield study. *Ann Rheum Dis* 74(6):1072–1077. <https://doi.org/10.1136/annrheumdis-2013-205095>
 16. Jia E, Zhu JQ, Huang WH et al (2018) Dual-energy computed tomography has limited diagnostic sensitivity for short-term gout. *Clin Rheumatol* 37(3):773–777. <https://doi.org/10.1007/s10067-017-3753-z>
 17. Zhang BH, Xu HL, Chen J et al (2021) Highly specific and label-free histological identification of microcrystals in fresh human gout tissues with stimulated Raman scattering. *Theranostics* 11(7):3074–3088. <https://doi.org/10.7150/thno.53755>
 18. Hu FH, Shi LX, Min W (2019) Biological imaging of chemical bonds by stimulated Raman scattering microscopy. *Nat Methods* 16(9):830–842. <https://doi.org/10.1038/s41592-019-0538-0>
 19. Xu H, Zhang B, Chen Y et al (2023) Type II collagen facilitates gouty arthritis by regulating MSU crystallisation and inflammatory cell recruitment. *Ann Rheum Dis* 82(3):416–427. <https://doi.org/10.1136/ard-2022-222764>
 20. Zhao Z, Su HF, Zhang PF et al (2017) Polyene bridged AIE luminogens with red emission: design, synthesis, properties and applications. *J Mater Chem B* 5(8):1650–1657. <https://doi.org/10.1039/C7TB00112F>
 21. Qian J, Tang BZ (2017) AIE luminogens for bioimaging and theranostics: from organelles to animals. *Chem* 3(1):56–91. <https://doi.org/10.1016/j.chempr.2017.05.010>
 22. Mei J, Leung NLC, Kwok RTK et al (2015) Aggregation-induced emission: together we shine, united we soar! *Chem Rev* 115(21):11718–11940. <https://doi.org/10.1021/acs.chemrev.5b00263>
 23. Niu GL, Zhang RY, Shi XJ et al (2019) AIE luminogens as fluorescent bioprobes. *Trends Analyt Chem* 123:115769. <https://doi.org/10.1016/j.trac.2019.115769>
 24. Cai YF, Ji X, Zhang YS et al (2022) Near-infrared fluorophores with absolute aggregation-caused quenching and negligible fluorescence re-illumination for in vivo bioimaging of nanocarriers. *Aggregate* 4(2):16. <https://doi.org/10.1002/agt2.277>
 25. Wang YQ, Xia BZ, Huang QQ et al (2021) Practicable applications of aggregation-induced emission with biomedical perspective. *Adv Healthc Mater* 10(24):e2100945. <https://doi.org/10.1002/adhm.202100945>
 26. Dong YS, Liu B, Yuan YY (2018) AIEgen based drug delivery systems for cancer therapy. *J Control Release* 290:129–137. <https://doi.org/10.1016/j.jconrel.2018.09.028>
 27. Xia F, Wu J, Wu X et al (2019) Modular design of peptide- or DNA-modified AIEgen probes for biosensing applications. *Acc Chem Res* 52(11):3064–3074. <https://doi.org/10.1021/acs.accounts.9b00348>
 28. Khan IM, Niazi S, Khan MKI et al (2019) Recent advances and perspectives of aggregation-induced emission as an emerging platform for detection and bioimaging. *Trends Analyt Chem* 119:115637. <https://doi.org/10.1016/j.trac.2019.115637>
 29. He W, Zhang TF, Bai HT et al (2021) Recent advances in aggregation-induced emission materials and their biomedical and healthcare applications. *Adv Healthc Mater* 10(24):e2101055. <https://doi.org/10.1002/adhm.202101055>
 30. Gu MJ, Zeng ZX, Xing M et al (2019) The biological applications of two aggregation-induced emission luminogens. *Biotechnol J* 14(12):e1900212. <https://doi.org/10.1002/biot.201900212>
 31. Zhang GQ, Feng WW, Gao ZY et al (2023) A NIR ratiometric fluorescent biosensor for sensitive detection and imaging of α -L-fucosidase in living cells and HCC tumor-bearing mice. *Aggregate* 4:e286. <https://doi.org/10.1002/agt2.286>
 32. Coderre TJ, Wall PD (1987) Ankle joint urate arthritis (AJUA) in rats: an alternative animal model of arthritis to that produced by Freund's adjuvant. *Pain* 28(3):379–393. [https://doi.org/10.1016/0304-3959\(87\)90072-8](https://doi.org/10.1016/0304-3959(87)90072-8)
 33. Tang PP, Wang YB, Wang KY (2020) Preparation of high-efficiency near-infrared aggregation-induced emission nanoparticles based on FRET and their use in bio-imaging. *Methods Appl Fluoresc* 8(1):015007. <https://doi.org/10.1088/2050-6120/ab6704>
 34. Jiang Y, Hadjichristidis N (2021) Diels-alder polymer networks with temperature-reversible cross-linking-induced emission. *Angew Chem Int Ed Engl* 60(1):331–337. <https://doi.org/10.1002/ange.202013183>
 35. Medina Rivero S, García Arroyo P, Li L et al (2021) Single-molecule conductance in a unique cross-conjugated tetra(aminoaryl)ethene. *Chem Commun* 57(5):591–594. <https://doi.org/10.1039/D0CC07124B>
 36. Nie MZ, Yang L, Zhao C et al (2019) A luminescent single-molecule magnet of dimetallofullerene with cage-dependent properties. *Nanoscale* 11(40):18612–18618. <https://doi.org/10.1039/c9nr05255k>
 37. Wang QY, Ke WQ, Lou HY et al (2021) A novel fluorescent metal-organic framework based on porphyrin and AIE for ultra-high sensitivity and selectivity detection of Pb²⁺ ions in aqueous solution. *Dyes Pigm* 196:109802. <https://doi.org/10.1016/j.dyepig.2021.109802>
 38. Miao YM, Yang WL, Lv JZ (2020) Fluorescence detection of fluorine ions in biological fluids based on aggregation-induced emission. *RSC Adv* 10(47):28205–28212. <https://doi.org/10.1039/d0ra03791e>
 39. Li CQ, Zhang J, Zhang SY et al (2019) Efficient light-harvesting systems with tunable emission through controlled precipitation in

- confined nanospace. *Angew Chem Int Ed Engl* 58(6):1643–1647. <https://doi.org/10.1002/anie.201812146>
40. Liu CC, Bai HT, He BZ et al (2021) Functionalization of silk by AIEgens through facile bioconjugation: full-color fluorescence and long-term bioimaging. *Angew Chem Int Ed Engl* 60(22):12424–12430. <https://doi.org/10.1002/anie.202015592>
 41. Pessler F, Mayer CT, Jung SM et al (2008) Identification of novel monosodium urate crystal regulated mRNAs by transcript profiling of dissected murine air pouch membranes. *Arthritis Res Ther* 10(3):R64. <https://doi.org/10.1186/ar2435>
 42. Liu-Bryan R, Scott P, Sydlaske A et al (2005) Innate immunity conferred by Toll-like receptors 2 and 4 and myeloid differentiation factor 88 expression is pivotal to monosodium urate monohydrate crystal-induced inflammation. *Arthritis Rheum* 52(9):2936–2946. <https://doi.org/10.1002/art.21238>
 43. Zamudio-Cuevas Y, Martinez-Nava GA, Martinez-Flores K et al (2021) Synovial fluid analysis for the enhanced clinical diagnosis of crystal arthropathies in a tertiary care institution. *Clin Rheumatol* 40(8):3239–3246. <https://doi.org/10.1007/s10067-021-05610-0>
 44. Ruban TN, Albert L (2015) Wrist involvement of calcium hydroxyapatite deposition disease. *J Rheumatol* 42(9):1724–1725. <https://doi.org/10.3899/jrheum.150178>
 45. Doumas C, Vazirani RM, Clifford PD et al (2007) Acute calcific periarthritis of the hand and wrist: a series and review of the literature. *Emerg Radiol* 14(4):199–203. <https://doi.org/10.1007/s10140-007-0626-9>
 46. Park S, Lee LE, Kim H et al (2021) Detection of intracellular monosodium urate crystals in gout synovial fluid using optical diffraction tomography. *Sci Rep* 11(1):10019. <https://doi.org/10.1038/s41598-021-89337-7>
 47. Huber FA, Gkoumas S, Thuring T et al (2020) Detection and characterization of monosodium urate and calcium hydroxyapatite crystals using spectral photon-counting radiography: a proof-of-concept study. *Eur J Radiol* 129:109080. <https://doi.org/10.1016/j.ejrad.2020.109080>

Springer Nature or its licensor (e.g. a society or other partner) holds exclusive rights to this article under a publishing agreement with the author(s) or other rightsholder(s); author self-archiving of the accepted manuscript version of this article is solely governed by the terms of such publishing agreement and applicable law.